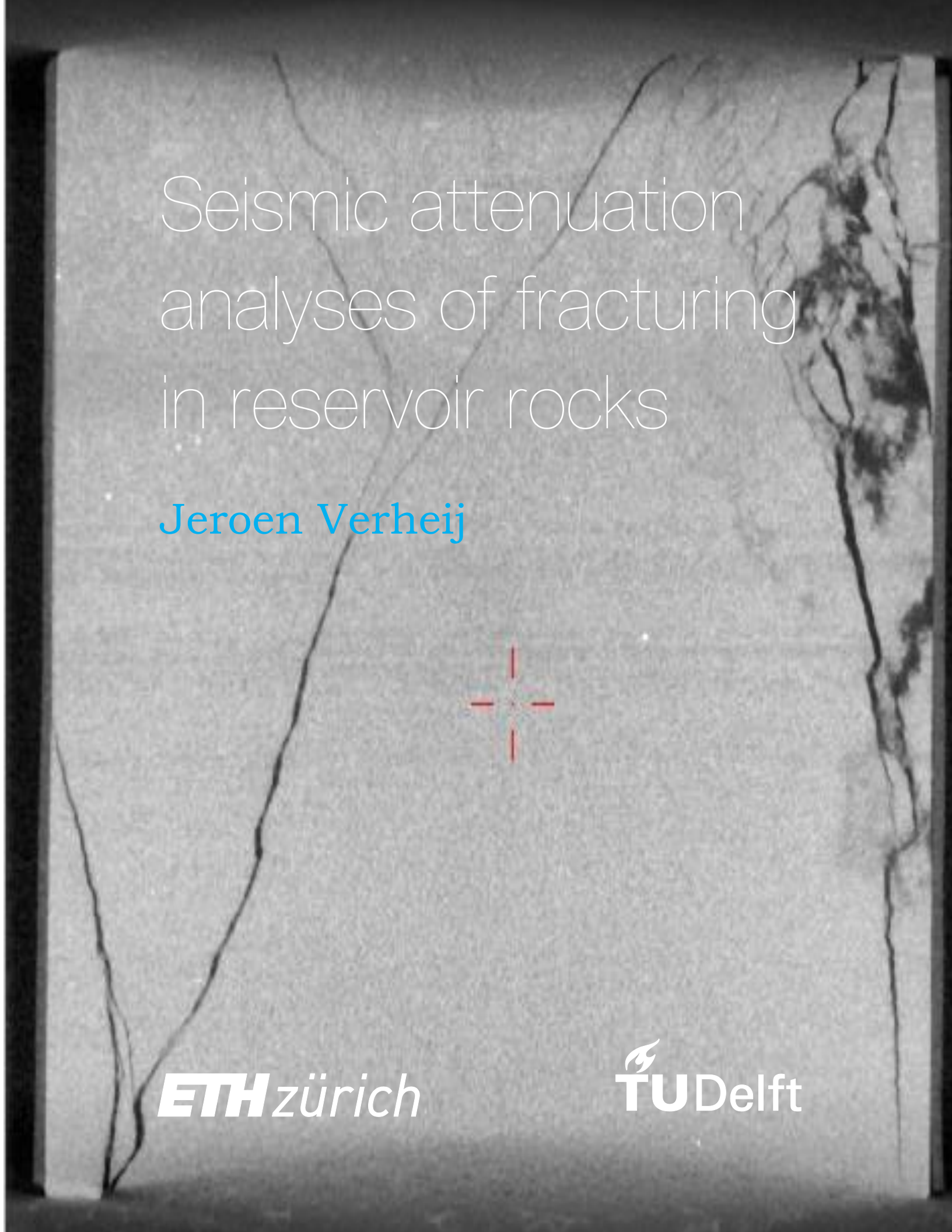
Seismic attenuation analyses of fracturing in reservoir rocks
Jeroen Verheij
ETH zürich
TU Delft

Seismic attenuation analyses of fracturing in reservoir rocks

By

Jeroen Verheij

in partial fulfilment of the requirements for the degree of

Master of Science

in Petroleum Engineering and Geosciences

at Delft University of Technology,
to be defended publicly on Tuesday 18th of August 2015 at 11:00.

Supervisor:	Dr. A. Barnhoorn	
Thesis committee:	Prof. dr. P.L.J. Zitha	TU Delft
	Prof. dr. G. Bertotti	TU Delft
	Dr. M. Frehner	ETH Zurich

TU Delft Delft University of Technology

Abstract

In this study seismic wave velocity and seismic wave attenuation in dry Bentheimer sandstone, Indiana limestone, and Whitby shale are studied while continuously deforming and therefore increasingly fracturing the rock samples up until macroscopic failure. A pulse transmission technique at a central frequency of 1 MHz is used in combination with a high pressure system that is constantly applying uniaxial stress. At early deformation stages before yielding, increasing elastic strains correlate with decreasing seismic attenuation suggesting closure of existing fractures. The deviation from a linear stress-strain relationship indicates the yield point, i.e. the onset of plasticity or fracturing. After yielding, increasing plastic strains correspond to increasing seismic attenuation suggesting formation of new micro-fractures. Thereby, P-wave attenuation is more sensitive to the growth of fractures than S-wave attenuation. The existence of fractures is confirmed by postmortem micro-CT-images. Absolute attenuation values are highest for Indiana limestone and lowest for Whitby shale. Furthermore, S-wave attenuation is the most sensitive to fracturing in Indiana limestone, followed by Bentheimer sandstone; P-wave attenuation is the most sensitive to fracturing in Bentheimer sandstone, followed by Indiana limestone. Attenuation in Whitby shale is the least sensitive to fracturing for both P- and S-waves. This study confirms that attenuation is more sensitive to fracturing than the seismic velocity; hence attenuation is suggested to be a valuable seismic property to identify fractures. At last, the study presents the possible usage of amplitude decay-over-time analysis of seismic waves for possible borehole applications.

Acknowledgements

This thesis could not have been written without the help of some wonderful people and organizations. This page is devoted to make an attempt to show my graduate.

First of all, I would like to thank Dr. Auke. Barnhoorn, my supervisor. Throughout the entire process of writing this thesis, Auke continuously supported me with information, ideas and enthusiasm. I wouldn't be able to write this thesis without his guidance.

Secondly, Prof. dr. P.L.J. Zitha, chair of the assessment committee, is acknowledged for his support and critiques. Furthermore, I would also like to thank the other members of my thesis committee: Prof. dr. G. Bertotti and in particular Dr. Marcel Frehner. I would like to thank Marcel. my supervisor at ETH Zurich, for offering the unique experience of studying in Switzerland, for being a continuous source of ideas and information and for always being available for answering numerous questions.

The assistance provided by the Geoscience & Engineering lab technicians at TU Delft, especially Wim Verwaal and Karel Heller, is greatly appreciated. Despite the countless requests to set up a new measurement, these men were always willing to help.

Special thanks to 'Stichting Molengraaff Fonds' that financially supported my research.

Last, I would like to thank my family and friends for their continuously support and encouragement throughout my study.

Contents

Figures

Tables

1. Introduction

Hydraulic fracturing is used in hydrocarbon reservoirs to provide pathways that allow hydrocarbons to reach the well bore. For example, production in the Netherlands form conventional resources like the Groningen gas field is rapidly declining. The Groningen gas field is expected to hardly produce anything anymore by 2025–2030 [*Zijp*, 2012]. The Lower Jurassic (Toarcian) Posidonia Shale Formation (PSF) is a possible candidate for shale gas production. However, due to its low permeability, hydraulic fracturing is inevitable in order to produce shale gas economically [*Britt and Schoeffler*, 2009]. The amount of gas that can be recovered from shale depends on the success of hydraulic fracturing activities, which are in turn influenced by the mechanical properties of the reservoir rocks [*Zijp*, 2013]. Therefore, reservoir characteristics such as seismic anisotropy or the topology of fracture networks in shales or in other tight reservoir rocks are of great interest to hydrocarbon exploration and production [*Samec and Blangy*, 1992].

The presence of fractures alters the propagation behavior of seismic waves (i.e., velocity dispersion and attenuation). Seismic velocities at high stress levels decrease at an increasing rate with increasing differential stress, which is generally attributed to the opening of cracks [*Lockner et al.*, 1977; *Scott et al.*, 1992]. Tocher [1957] suggested that these changes in seismic velocities could indicate that rock failure is imminent, providing a way to predict both rock bursts in mines and earthquakes on faults.

The presented study focusses on seismic wave attenuation (i.e., decay of seismic waves), which is referred to as the inverse of the quality factor Q and is related to the energy loss per cycle. Winkler [1979] has found that seismic wave attenuation is much more sensitive to rock properties than seismic wave velocity (denoted *v*). Attenuation measurements may enable the identification of subsurface characteristics such as the orientation of fractures, the anisotropic permeability of shale, whether fractures are open or closed, or the pore fluid content and its corresponding saturation [*Maultzsch et al.*, 2003, 2007; *Chichinina et al.*, 2006].

Toksoz *et al.* [1979] described a laboratory method to measure seismic attenuation. The effect of anelastic behavior of rocks leading to a reduction of seismic wave amplitude is called intrinsic attenuation. The amplitude of the first arrival is recorded and compared with a reference material. This comparison allows calculating the attenuation of the seismic wave. A lot of research focused on ultrasonic wave propagation as a function of stress prior to the onset of plasticity (start of fracturing) [*Mavko and Nur*, 1979; *Christensen and Wang*, 1985; *Khaksar et al.*, 1999]. For the elastic regime, attenuation decreases with increasing effective stress, presumably due to crack closure [*Winkler*, 1982]. The effects of heterogeneities and anisotropy in rocks are studied by Lucet and Zinszner [1991] and found that values for Q_s^{-1} are bigger than Q_p^{-1} due to shear wave splitting.

On the other hand, there is little known about seismic wave propagation during fracturing. Stanchits, Vinciguerra, & Dresen [2006] have shown that immediately before failure, v_p and v_s decrease significantly for a granite rock sample. For a limestone rock sample, [*Couvreur et al.*, 2001] showed that S-wave attenuation increases before failure at high stress levels.

The aim of his study is to perform *P*-wave and *S*-wave attenuation measurements before and during fracturing for multiple reservoir rock samples, from the early elastic deformation regime to the development of a fully connected macroscopic fracture network. The attenuation characteristics due to the developing fractures may eventually be used to better describe fractured reservoirs and may help to detect when rock bodies approach failure.

2. Materials and Methods

Rock samples

In this study, three different rock types are used: Bentheimer sandstone, Indiana limestone, and Whitby shale. From the block of Bentheimer sandstone and Indiana limestone, rock samples are cut in the same direction. Possible effects of anisotropy are therefore the same in all Bentheimer sandstone and Indiana limestone rock samples. Whitby shale has water-phobic nature and due to its fragility , Whitby shale samples are sawed manually from blocks of shale and manually polished to cylindrical rock samples. All Whitby shale samples are horizontally layered.

The homogenous Bentheimer sandstone has a density of 2.67 g/cm^3 and is used because of its high porosity of 24.7% and high permeability of 2.4 mD [*Maloney et al.*, 1990]. The sandstone is mined in quarries in the County of Bentheim in Germany. It is the same formation as the reservoir rock from the Schoonebeek oil field [*Klein et al.*, 2001]. Grain sizes predominantly range from fine to medium sand, but up to granule sizes occur. The sandstone is assumed to be homogenous and isotropic.

Indiana limestone (also known as the Salem limestone) is a calcite-cemented grainstone formed from fossil fragments and oolites [*INDIANA-LIMESTONE-INSTITUTE-OF-AMERICA*, 2007]. The limestone was ordered at Kocourek-Industries [2013]. It is assumed to be homogenous, has a porosity of 19% and a permeability of 70 mD. A density of 2.69 g/cm^3 is determined by Miller and Florence [1991].

The heterogeneous and anisotropic Whitby shale is the rock with the lowest density, porosity, and permeability. Whitby shale is a member of the PSF [*Boogaert and Kouwe*, 1993]. An outcrop of this formation can be found in Whitby, UK, and the origin of the shale samples that are used in this study is presented in Figure 1 [*Google-Earth*, 2015]. The studies of Lie-A-Fat [2014] and Ravestein [2014] on a majority of the same shale samples have found densities of 2.25–2.55 g/cm^3 and porosities of 0.5%–2.5% and the study of Houben et al. [2015] has found a gas permeability of 0.02–1*10^{-5} mD. The rock characteristics of all the rock samples that are found in previous studies are summarized and presented

in


Port Mulgrave
187 m
© 2015 Infoterra Ltd & Bluesky
Google earth

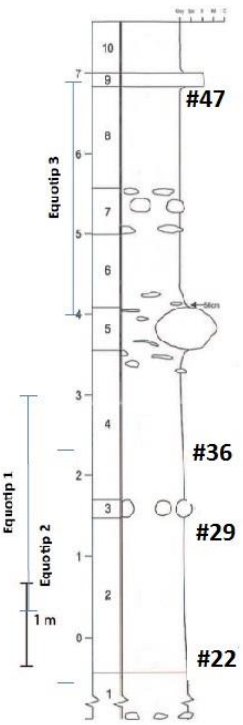
Equotip 3
Equotip 1
Equotip 2
1 m
#47
#36
#29
#22

Table 1.

Figure 1. Left: shale outcrop in Whitby, United Kingdom [*Google-Earth*, 2015]. Right: Stratigraphic column of the WMF near Whitby, U.K. (Courtesy of Linde van Laerhoven) with sample indication that are used in this study. The left axis shows the height in m next to the three Equotip sections.

Table 1: Overview of the main rock characteristics (density, porosity and permeability) of the three rock samples

rock sample	ρ **(g/cm^3)**	ϕ **(%)**	κ **(mD)**
Bentheimer sandstone	2.67	24.7	2.4 (brine)
Indiana limestone	2.69	19	70 (brine)
Whitby shale	2.25–2.55	0.5–2.5	0.02–1*10^{-5} (gas)

All the cylindrical samples that were cored (Bentheimer sandstone and Indiana limestone), have a diameter of 40±0.5 mm and were cut into pieces with a length of 32±0.5 mm. Whitby Shales (that were polished have a diameter of 40±0.5 mm and were cut into pieces with a length ranging from 27±0.5 mm to 41±0.5 mm.

The American Society for Testing and Materials (A.S.T.M.) standard for uniaxial compressive tests specifies that the rock samples should be at least 2 inches high with a height-to-width ratio, L/D, of $L/\mathrm{D} \geq 1$. There is ample evidence that apparent uniaxial compressive strength decreases as L/D increases [*Hawkes and Mellor*, 1970]. The probable sequence of internal crack formation and the relative crack density in the early stages of fracturing can be inferred. Figure 2 (retrieved from [*Hawkes and*

Mellor, 1970]) shows that cracking in rock samples with a height to width ratio $L/\mathrm{D} \approx 2.5$ is most unlikely in the dome-shaped regions abutting the loading platens; the most critically stressed zones lie between these regions of low crack probability and the central cross-section, and also around the perimeter of the platen contact [*Hawkes and Mellor*, 1970; *Paterson and Wong*, 2005].

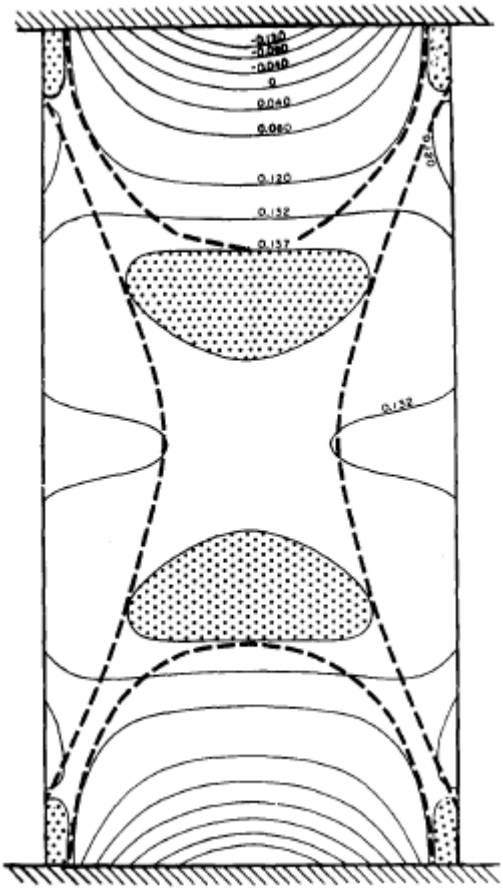

Figure 2: Contours of the McClinstock-Walsh parameter, *C*, for uniaxial compression with radial restraint at the sample ends. The numbers give the magnitude of *C* as a multiple of the mean axial stress, shaded areas show the most critically stressed zones and the broken lines indicate a probable pattern for the final collapse of the specimen [*Hawkes and Mellor*, 1970].

Due to the limitations of the experimental setup, rock samples with $L/\mathrm{D} \leq 1$ are used. However, the focus of this study is not on the dynamic moduli of the rock samples. Instead, the focus is on the propagation of seismic waves through the rock samples.

Experimental setup

The unconfined compressive strength (UCS) test is of great importance to get an idea of the fracture growth, its orientation before and after the macroscopic failure and the maximum stress that a sample can sustain. This knowledge is essential in many theoretical and practical applications, particularly in hydraulic fracturing problems.

An overview of the exeperimental setup is presented in Figure 3. The ultrasonic experiments are conducted at ambient condition. To mimic in-situ conditions and study elastic wave propagation through the rock samples, a ultrasonic setup is integrated within a high-pressure system [*Zhubayev and Barnhoorn*, 2013], which can apply a vertical force up to 500 kN. The rock sample is placed between two

aluminum buffers. Ultrasonic *P*-wave and *S*-wave transducers (one transmitter and one receiver) are coupled on each buffer with a viscous gel and held in contact by springs. The transducer's central frequency is 1 MHz. A differential stress can be applied to the aluminum buffers and in this way *P*-wave and *S*-wave velocity and attenuation of the rock samples are studied during ongoing compression. All rock samples are dried and jacketed with heat-shrink tubing prior to the ultrasonic experiment to ensure that the rock sample does not completely fall apart, so the fractures can later be analyzed by a CT-scan. The result of the (vertical) stress as a function of (vertical) strain is presented in Figure 4a.

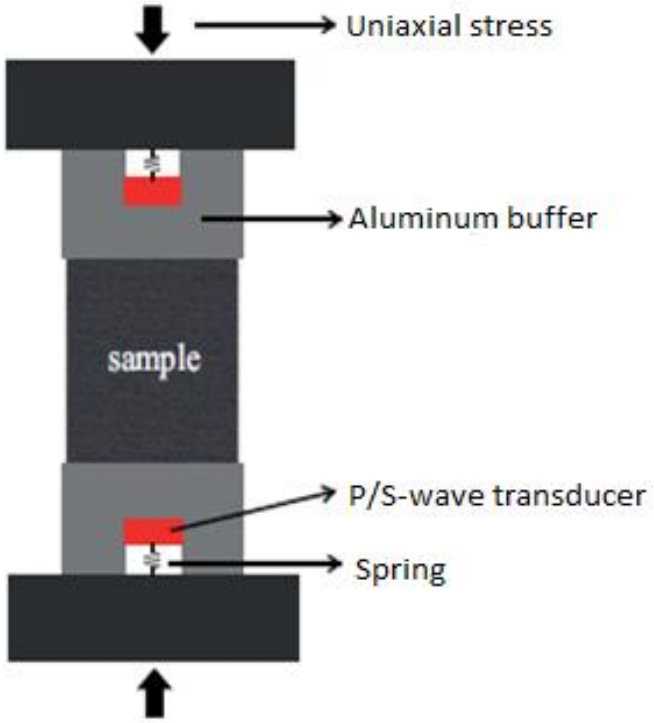

Figure 3: Schematic overview of the experimental setup used to measure velocity and attenuation at different uniaxial stress levels.

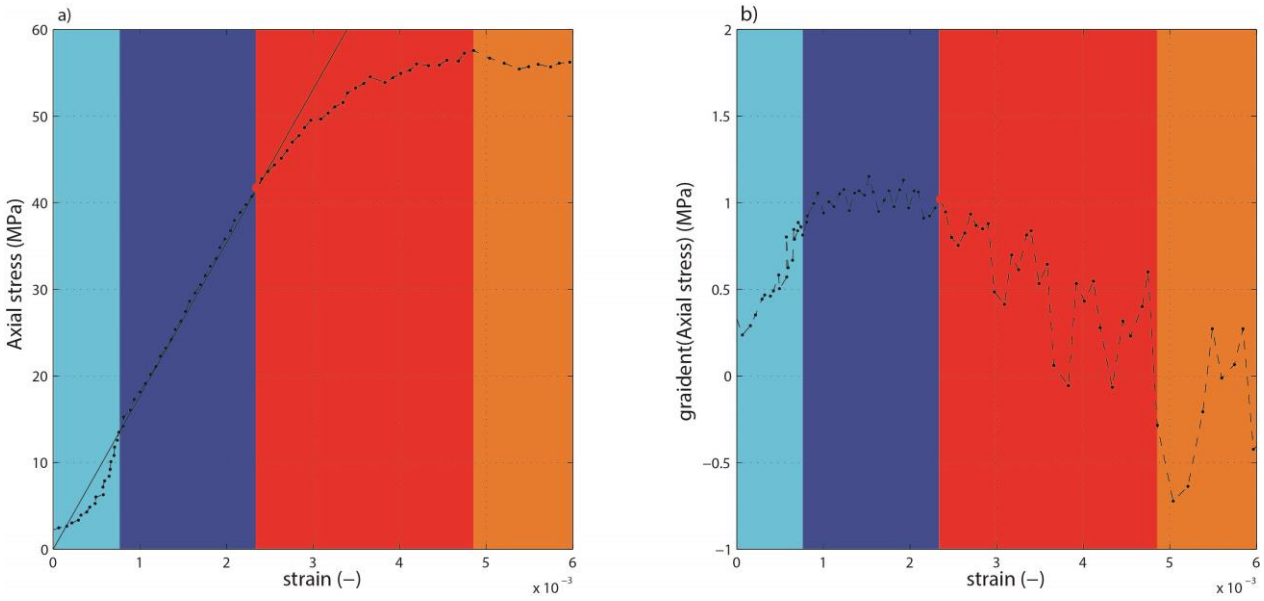

Figure 4. a) Vertical stress as a function of vertical strain. The yield point is presented in red that is computed in b). Additionally, the tangent is drawn for the computation of the Young's modulus. b) Gradient of vertical stress as a function of vertical strain.

Four regimes are identified in Figure 4: the initial part (non-linear part due to coupling of the system) in cyan, the elastic regime in blue, the plastic regime in red, and the completely fractured regime in orange. When the axial stress is approaching the maximum uniaxial strength of the rock, the slope of the stress-strain curve decreases. This effect is associated with the formation of microcracks, which progressively destroy the load-bearing capability of the rock and permit irreversible strain to occur [*Hawkes and Mellor*, 1970]. The point where the stress-strain curve deviates from a linear relationship is called the yield point and is represented in red in Figure 4b. The yield point is determined by the onset of the decrease of the gradient curve that is presented in Figure 4b. Barnhoorn et al. [2010] have shown that for increasing deformation up to peak stress conditions, the formation of fractures is marked by an increasing number of individual fractures. Therefore, in this study the yield point is interpreted as the onset of fracturing of the rock samples. In Figure 4c the stress-strain relationship is presented again with the corresponding yield point. Additionally, the tangent (and therefore the Youngs modulus, E) is drawn in the linear regime of the experiment. The linear regime starts after the initial nonlinear effects caused by coupling of the system and lasts up to the yield point.

Signal processing

Velocity measurements are carried out by dividing the deformed sample length by the first arrival time:

$$v = \frac{l_0 - dl}{t_{first}}, \tag{1}$$

where l_0 is the original rock sample length, dl is the shortening of the rock sample, and t_{first} is the first arrival time of the seismic wave (Figure 5). An algorithm is used to automatically pick the first arrival of *P*-wave and *S*-waves guaranteeing consistency of the velocity analyses.

To improve the accuracy of the arrival time picking, more data points are needed than are sampled; hence upsampling is applied to increase the data density as follows. First, n-1 zeros (with n equal to the original length of the dataset) are inserted into the data trace between the original data points. Next, a linear interpolation replaces the zeros by the average of the neighboring data points. The new data trace has now twice the data density as the original one, but without changing the behavior the seismic signal (Figure 5). *P*-waves are upsampled two times and *S*-waves are upsampled three times.

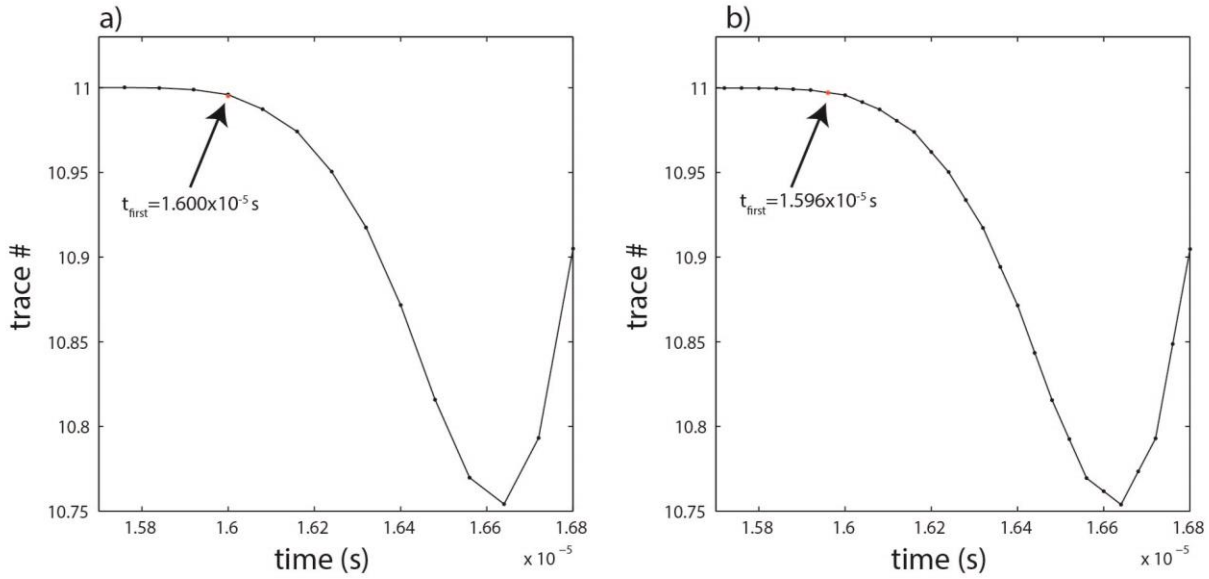

Figure 5: Seismic trace of a *P*-wave in Bentheimer sandstone. a) Only a limited amount of data points (black dots) are available for the picking of the first arrival. b) Upsampled dataset: more data points are available to pick the first arrival of the *P*-wave.

Attenuation calculations are performed by the spectral ratio method proposed by Toksoz *et al.* [1979] using a pulse transmission technique. The attenuation is measured relatively to a reference sample which has negligible attenuation.

The amplitudes of plane seismic waves for the rock sample and the reference sample can be expressed as

$$A_1(f) = G_1(s) e^{-\alpha_1(f)s} e^{i(2\pi ft - k_1 s)}, \tag{2}$$

$$A_2(f) = G_2(s) e^{-\alpha_2(f)s} e^{i(2\pi ft - k_2 s)}, \tag{3}$$

where A is the amplitude, f is the frequency, s is the distance, $k = 2\pi / f$ is the wavenumber, v is the velocity, $G(s)$ is a geometrical factor, which includes spreading, reflections etc., and $a(f)$ is the frequency-dependent attenuation coefficient. The subscripts 1 and 2 refer to the reference and the rock sample respectively. If the assumption is made that over the frequency range of the measurements (0.1–1 MHz), α is a linear function of the frequency, the frequency-dependent attenuation coefficient can be defined as

$$\alpha(f) = \beta f, \tag{4}$$

where β is constant and related to the quality factor, Q. The definition of Q is given as

$$Q = \frac{\pi}{\beta v}. \tag{5}$$

When the same geometry is used for the reference and the sample (i.e., same dimensions, transducers, and arrangements), G_1 and G_2 are frequency-independent scale factors. Equation 6 represents the ratio of Fourier amplitudes:

$$\frac{A_1}{A_2} = \frac{G_1}{G_2} e^{-(\beta_1 - \beta_2)sf}. \tag{6}$$

Taking the natural logarithm of the ratio of the Fourier amplitudes yields

$$\ln\left(\frac{A_1}{A_2}\right) = (\beta_2 - \beta_1)sf + \ln\left(\frac{G_1}{G_2}\right), \tag{7}$$

where s is the propagating distance. In equation 7 the assumption is made that the rock sample and the reference sample have the exact same geometry. Due to the very low attenuation (Q^{-1}) of the reference sample (aluminum in this case, Q=150000), the constant β_1 in equation 7 is equal to zero. In Figure 6, the natural logarithm of the ratio of the two seismic waves is plotted as a function of frequency. Attenuation is determined from the tangent of the indicated line.

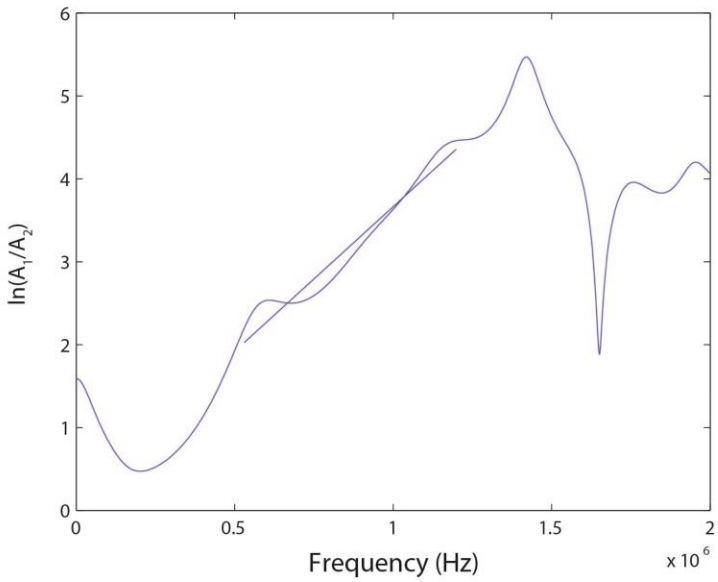

Figure 6: Natural logarithm of the ratio of the two seismic waves as a function of frequency. A_1 is the *P*-wave in Bentheimer sandstone and the A_2 is the *P*-wave in the reference sample.

3. Results

Rock characteristics

Prior to the deformation experiment, the rock samples are characterized by their physical properties. Mercury porosimetry is used to determine the pore size distribution of the rock samples. Pore diameters smaller than 0.1 nm and bigger than 0.1 mm are not detected by the mercury porosimeter. In Figure 7 the relative pore volume is presented as a function of the pore diameter, d , of Bentheimer sandstone, Indiana limestone, and Whitby shale sample 47 (see Figure 1). The dominant pore diameter of Whitby shale sample 47 (d_{shale}=22 nm) is much smaller compared to Bentheimer sandstone ($d_{sandstone}$=41 μm) and Indiana limestone ($d_{limestone}$=0.7 μm and 19 μm). The pore diameters in Whitby shale samples are a factor 1000 smaller than the pore diameters in Bentheimer sandstone and Indiana limestone and therefore yielding in a corresponding lower (a factor of 10,000 lower) permeability (see Table 2).
Furthermore, Bentheimer sandstone and Whitby shale sample 47 show one dominant pore diameter. Pore diameters are ranging from 0.1 μm to 100 μm for Bentheimer sandstone and from 4 nm to 10 μm for Whitby shale sample 47. On the other hand, Indiana limestone shows a bimodal distribution of the pore diameters. Pore diameters are ranging from 0.01 μm to 100 μm for Indiana limestone and two dominant pore diameters are found: $d_{limestone}$=0.7 μm and 19 μm.

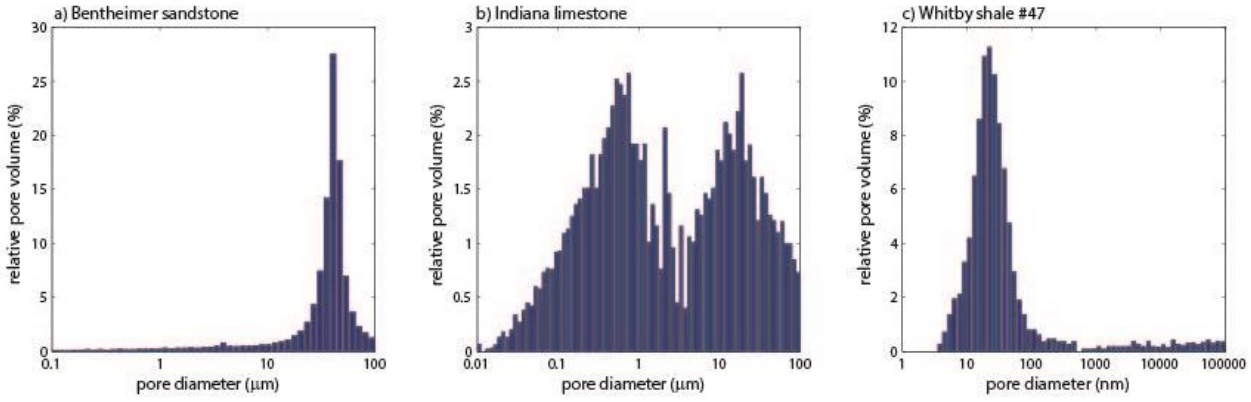

Figure 7: Pore size distributions of Bentheimer sandstone (a), Indiana limestone (b) and Whitby shale sample 47 (c).

A helium pycnometer analyzed the rock samples for density and porosity. The average density and average porosity for Bentheimer sandstone and Indiana limestone and the average Young's modulus, $\bar{E}$ (found from the UCS data), for all the rock samples are presented in Table 2.
Since the density, porosity and the Young's modulus are measured or computed multiple times and expressed in mean values, the corresponding uncertainty range of the mean is smaller than the

uncertainty range of a single given measurement. The uncertainty in the mean, Δx_{avg} (with x being the rock characteristic of interest, i.e. density, porosity of Youngs modulus), for small data sets (equation 8) is presented:

$$\Delta x_{avg} = \frac{x_{\max} - x_{\min}}{2\sqrt{N}}, \tag{8}$$

with $x_{\max}$ equal to the maximum value, $x_{\min}$ equal to the minimum value and N equal to the number of measurements.

To measure the density and porosity measurements of Whiby shales, the Whitby shales need to fit the gas pycnometer exactly and in this study is encountered to be a problem. Therefore, density and porosity values retrieved from *Lie-A-Fat* [2014] (a) and *Zhubayev and Barnhoorn* [2013] (b) on rock samples obtained of the same Whitby shale layer (Figure 1) are presented in Table 2. When the measurement Is performed on multiple rock samples of the same Whitby shale layer, the average density, $\bar{\rho}$, and average porosity, $\bar{\phi}$, are presented with the corresponding uncertainty in the mean.

Table 2: Overview of the results of the investigated rock characteristics for the three rock samples. Density and porosity values retrieved from *Lie-A-Fat* [2014] are indicated by (a) and Density and porosity values retrieved from *Zhubayev and Barnhoorn* [2013] are indicated by (b).

Rock sample	$\bar{\rho}$ **(g/cm^3)**	$\bar{\phi}$ **(%)**	$\bar{E}$ **(GPa)**
Bentheimer sandstone	2.65±0.0	24.0±0.5	18.9±1
Indiana limestone	2.69±0.0	17.8±0.4	12.5±5
Whitby shale	2.19±0.3[ab]	2.26±1[ab]	5.53±1
layer	$\bar{\rho}$ *or* ρ **(g/cm^3)**	$\bar{\phi}$ *or* ϕ **(%)**	$\bar{E}$ *or* E **(GPa)**
47	2.48±0.03[a]	2.40±0.2[a]	7.9±1
36	-	-	4
29	1.25±0.0[a]	0.68±0.3[a]	4.3
22	2.57[b]	4.7[b]	5.3±0.2

$\bar{\rho}$ and $\bar{\phi}$ of Bentheimer sandstone and of Indiana limestone are found with a small uncertainty. The uncertainty of the average Young's modulus of Bentheimer sandstone with respect to the value of

Young's modulus, $\left(\Delta E_{avg} / \bar{E}\right)_{B.sandstone}$=5.3% ,is quite small compared to that of Indiana limestone, $\left(\Delta E_{avg} / \bar{E}\right)_{I.limestone}$=40% and Whitby shale, $\left(\Delta E_{avg} / \bar{E}\right)_{W.shale}$=18%.

Furthermore, (average) density values of the Whitby shale layers are ranging from 1.25-2.57 g/cm^3 and (average) porosity values are ranging from 0.68—4.7%. Uncertainties with respect to the average value of Whitby shales obtained from layer 47 are: $\left(\Delta \rho_{avg} / \bar{\rho}\right)_{W.shale\ \#47}$=1.2%, $\left(\Delta \phi_{avg} / \bar{\phi}\right)_{W.shale\ \#47}$=8.3% and $\left(\Delta E_{avg} / \bar{E}\right)_{W.shale\ \#47}$=13%.

Velocity and attenuation results

In the Appendix the results of all the velocity and attenuation measurements of the high-pressure system coupled with the ultrasonic setup (Figure 3) are summarized for all the rock samples, whereas In Figure 8, Figure 9 and Figure 10 only two measurements (one *P*-wave and one *S*-wave) are presented per rock sample.

Uncertainties in the seismic velocity are added in quadrature [*Taylor*, 1982] for the computation of error bars:

$$\frac{\delta v}{|v|} = \sqrt{\left(\frac{\delta l}{l}\right)^2 + \left(\frac{\delta t_{first}}{t_{first}}\right)^2}, \tag{10}$$

whereas δv is the uncertainty in the velocity, v is the wave velocity, δl is the uncertainty in the sample length, l is the absolute sample length, δt_{first} is the uncertainty in the first arrival time, and t_{first} is the absolute first arrival time. The uncertainty in attenuation is a summation of the uncertainty in the velocity and β:

$$\frac{\delta Q^{-1}}{\left|Q^{-1}\right|} = \sqrt{\left(\frac{\delta \beta}{\beta}\right)^2 + \left(\frac{\delta v}{v}\right)^2}. \tag{11}$$

Uncertainties arise in the picking of the frequency band (FB) that is used for the linear fit (Figure 6). Changing the boundaries of the FB results in an uncertainty in the slope, $\frac{\delta \beta}{\beta}$, of approximately 2%, which is the uncertainty assigned to all values of β. The (non-presented) error bars for the velocity profiles are ranging from 1% to 2% and error bars for the attenuation profiles are ranging from 1% to 3%. Figure 8, Figure 9 and Figure 10 presents from top to bottom: the axial stress, wave velocity and attenuation (*P*-wave on the left, *S*-wave on the right) for Bentheimer sandstone, Indiana limestone and Whitby shales respectively. The yield point is marked in blue for the *P*-wave measurements and in red for the *S*-wave measurements.

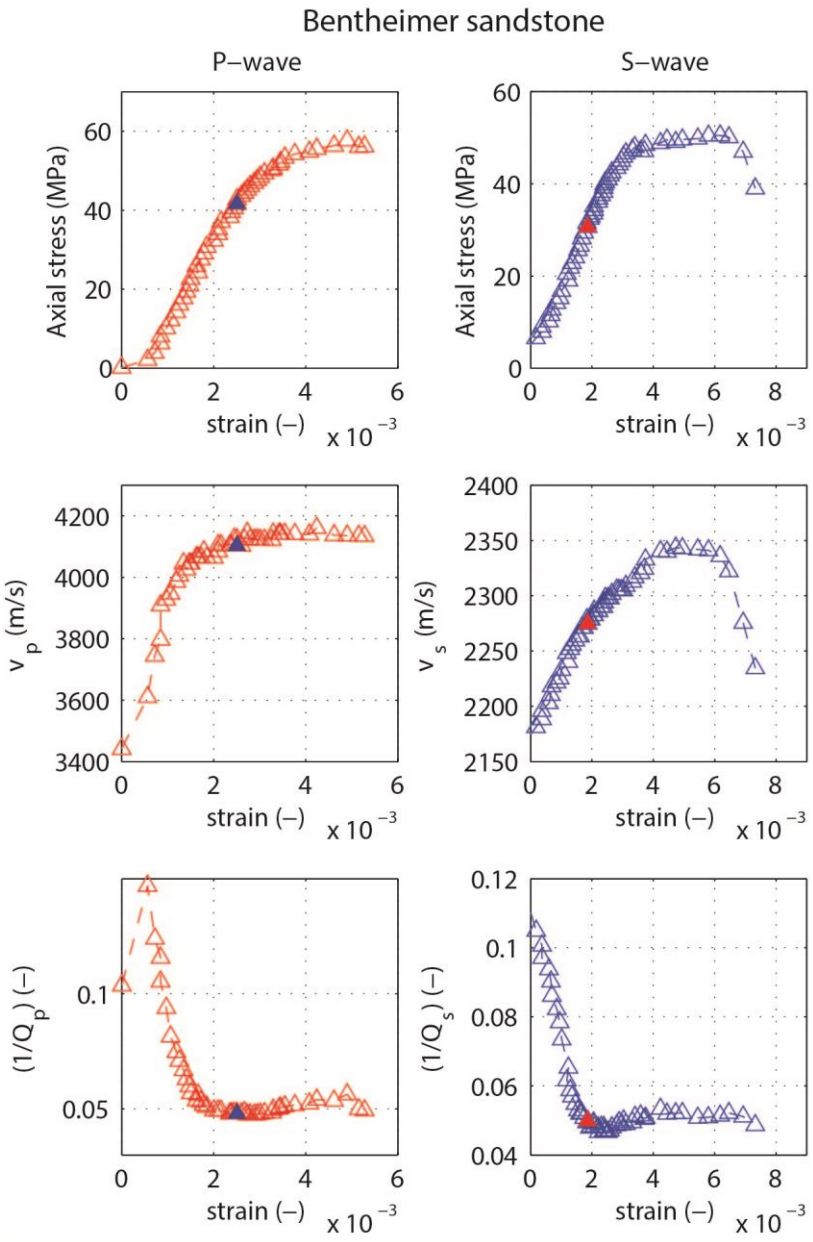

Figure 8: Axial stress (top), *P*-wave velocity (middle left), *S*-wave velocity (middle right), and *P*- and *S*-wave attenuation (bottom) of Bentheimer sandstone as a function of strain.

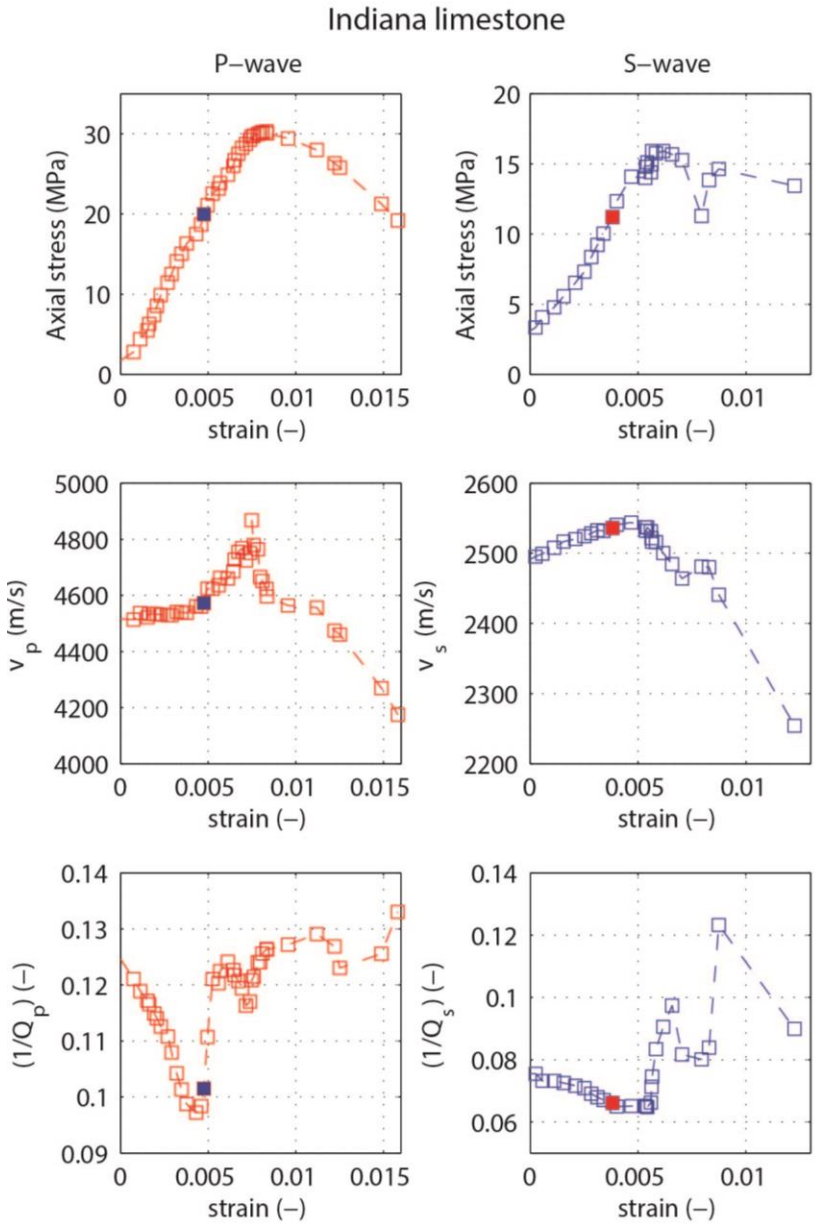

Figure 9: Axial stress (top), *P*-wave velocity (middle left), *S*-wave velocity (middle right), and *P*-wave and *S*-wave attenuation (bottom) of Indiana limestone as a function of strain.

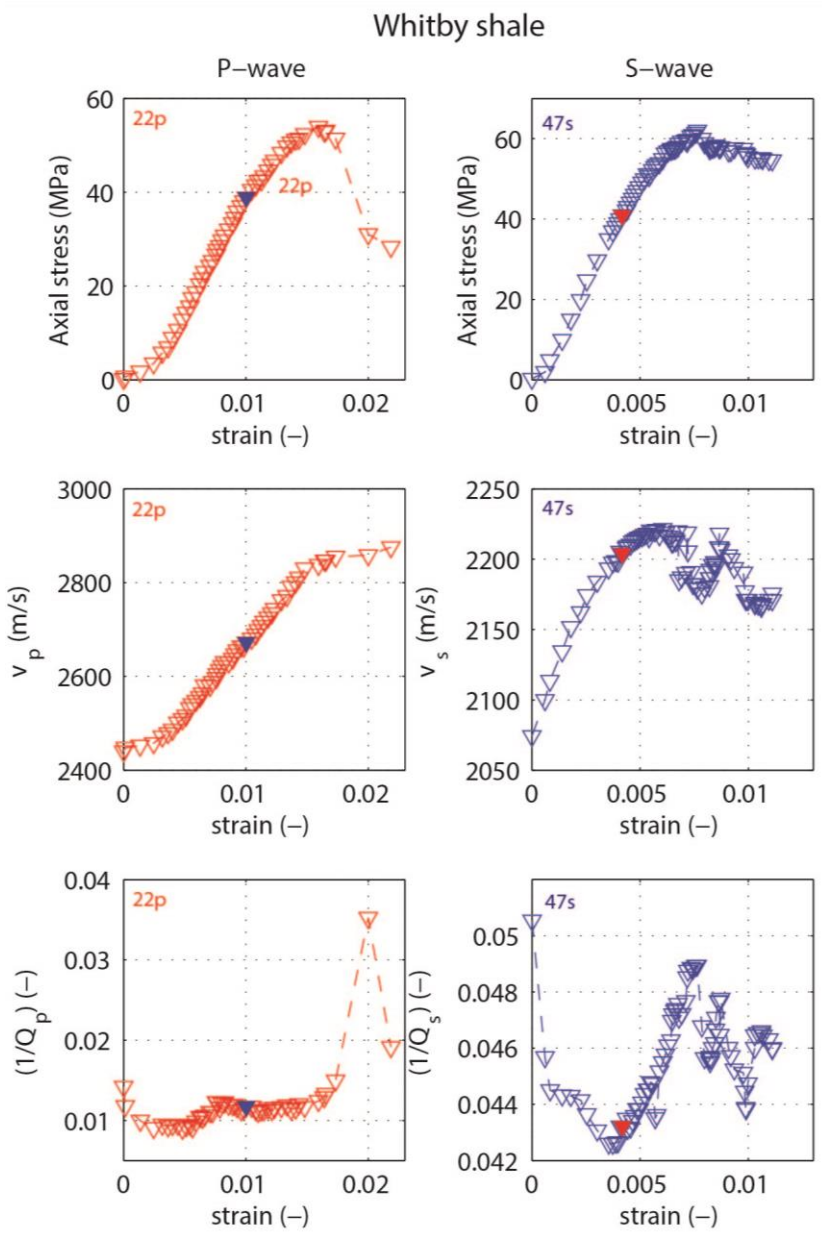

Figure 10: Axial stress (top), *P*-wave velocity (middle left), *S*-wave velocity (middle right), and *P*-wave and *S*-wave attenuation (bottom) of Whitby shale samples 22p and 47s as a function of strain.

The stress-strain relationships in Figure 8, Figure 9, and Figure 10 show that the resistance to deformation by axial stress of Bentheimer sandstone is larger compared to Indiana limestone and Whitby shale. The average Young's moduli of Indiana limestone, $\bar{E}$, are found to be 18.9±1 GPa, 12.5±5 GPa, and 5.52±1 GPa, respectively (Table 2). In addition, the strain between the peak stress and sample failure of Indiiana limestone is much larger compared to those of Bentheimer sandstone and Whitby shale. The maximum UCS, $\bar{\sigma}_{max}$, of Indiana limestone samples differs significantly in the three measurements. Values for $\bar{\sigma}_{max}$ of Indiana limestone are 37.5, 30.3 and 15.9 GPa, respectively.

Furthermore, the maximum *P*-wave and *S*-wave velocities, $v_{p,\max}$ and $v_{s,\max}$, of Whitby shale samples differ too: $v_{p,\max}$ ranges from 2857 to 3120 m/s and $v_{s,\max}$ ranges from 1552 to 2216 m/s. The velocities in the three rocks samples are sorted as: $v_{limestone} > v_{sandstone} > v_{shale}$ for both *P*-waves and *S*-waves and the absolute attenuation for the three rock samples are sorted as: $(Q^{-1}_{limestone}) > (Q^{-1}_{sandstone}) > (Q^{-1}_{shale})$ for both *P*-waves and *S*-waves.

In Figure 11 Whitby shale sample 36s is presented to clearly identify the effect of increasing strains on *S*-wave velocity and *S*-wave attenuation. Four regimes are identified in this figure: the initial part (non-linear part due to coupling of the system) in cyan, the elastic regime in blue, the plastic regime in red, and the completely fractured regime in orange.

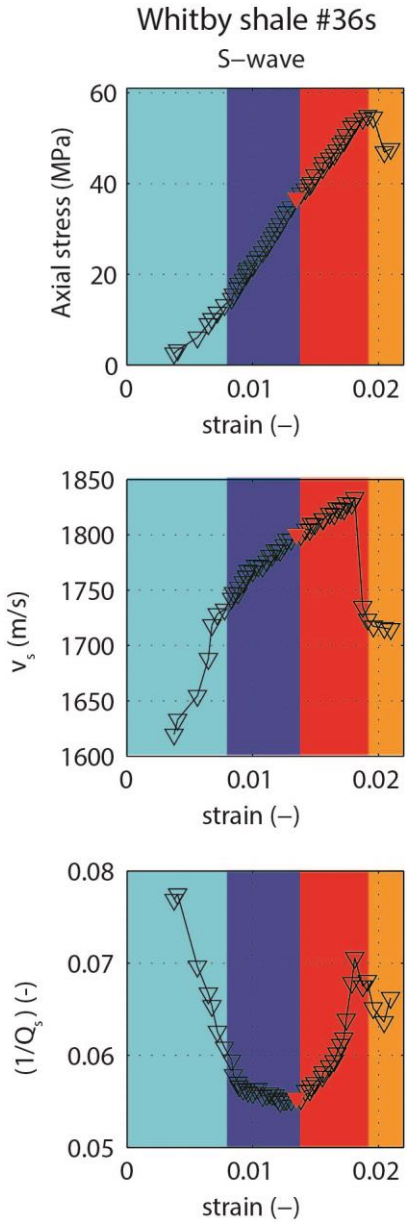

Figure 11: Axial stress (top), *S*-wave velocity (middle), and *S*-wave attenuation (bottom) as a function of strain of Whitby shale samples 36s.

Figure 11 reveals that in the initial (cyan) and elastic regime (blue) v_s is increasing from 1620 m/s to 1801 m/s with increasing strains. Simultaneously, Q_s^{-1} is decreasing from 0.077 to 0.055. The effect of decreasing attenuation with increasing elastic strains is also observed for *P*-waves (Figure 8, Figure 9, and Figure 10) for the other rock samples.

In the plastic regime (red) of Whitby shale sample 36s, v_s is further increasing with increasing plastic strains, whilst Q_s^{-1} is increasing from 0.055 to 0.068. This behavior is also observed for the other rock samples in Figure 8, Figure 9, Figure 10, and in the Appendix. All the results show increasing values for Q_p^{-1} and Q_s^{-1} for increasing plastic strains.

After the deformation experiments, the rock samples are analyzed using a micro-CT-scanner (Figure 12).

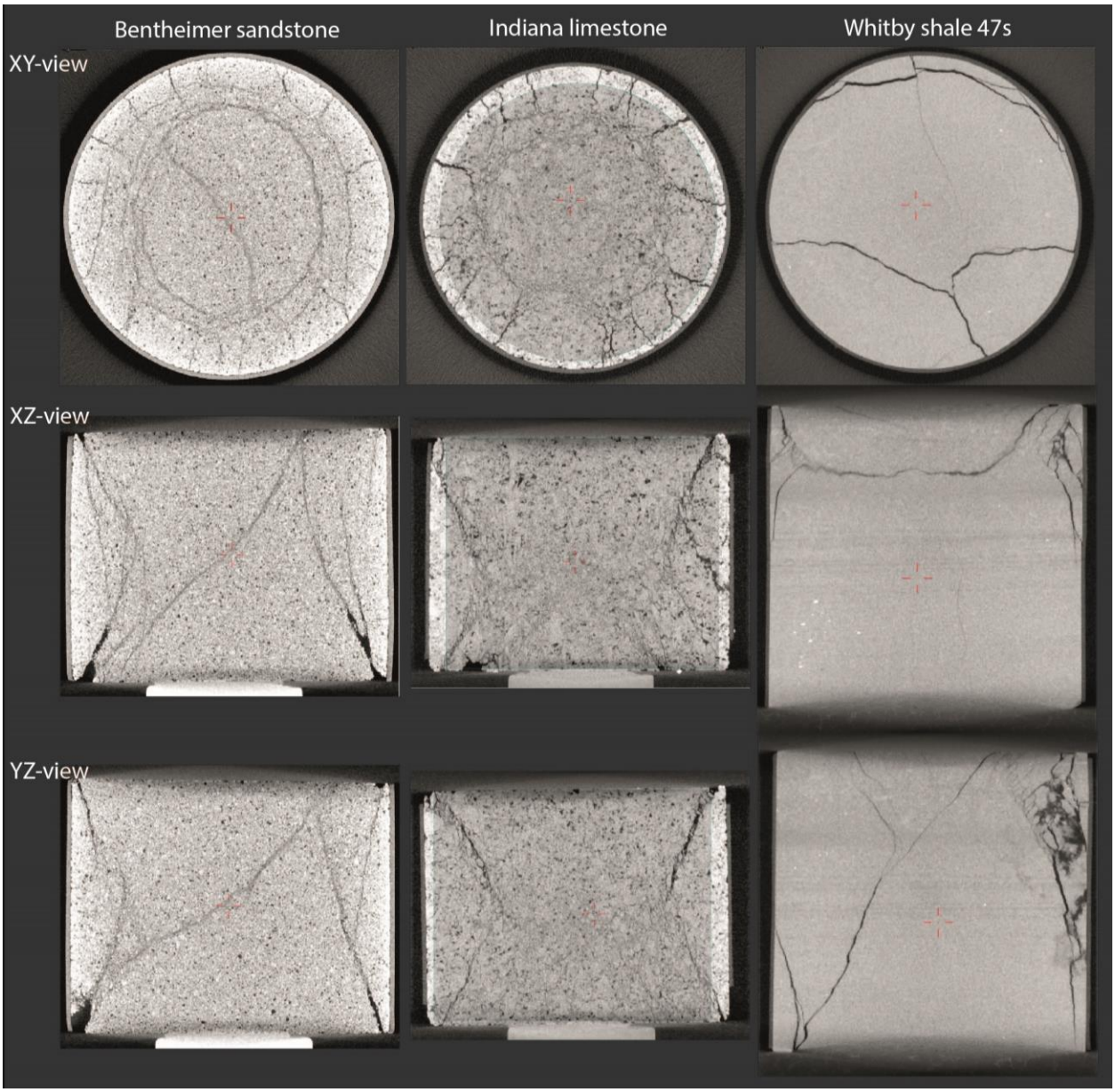

Figure 12: CT-scan images of the fractured rock samples: XY-view (top), XZ-view (middle) and YZ-view bottom) of Bentheimer sandstone (left), Indiana limestone (middle), and Whitby shale samples 47s (right).

The yield point is described as the onset of the formation of new microcracks [*Hawkes and Mellor*, 1970] and the number of such cracks increases with increasing deformation to peak stress conditions [*Barnhoorn et al.*, 2010]. The CT-scan images in Figure 12 show that all the rock samples are seriously damaged. The rock samples contain both small and big fractures. From the combination of the CT-scan images and the attenuation plots in Figure 8, Figure 9, and Figure 10, increasing plastic strains are interpreted as fracturing of the rock sample, which is associated with an increase in Q_p^{-1} and Q_s^{-1}.

After peak stress conditions (the orange regime in Figure 11), it is not possible to observe any general trends for velocity or attenuation. The rock sample is completely fractured (Figure 12). For Whitby shale

sample 36s, values for Q_s^{-1} decrease from 0.65 to 0.64 and increase again to 0.66. In particular, Q_p^{-1} and Q_s^{-1} of Indiana limestone (Figure 9) show a decrease in attenuation followed by an increase in attenuation for increasing strains after peak stress.

Whereas attenuation is increasing during the fracturing of rocks, a corresponding decrease in velocity could be expected. The contrary is observed in in Figure 11 for Whitby shale sample 36s: Q_s^{-1} is increasing from 0.055 to 0.068 and v_s is increasing from 1801 m/s to 1834 m/s, too; v_p of Indiana limestone and Whitby shale sample 22p also increase during fracturing. For Bentheimer sandstone an increase in attenuation during fracturing is observed, whereas v_p and v_s are constant.

Whitby shale sample 47p in the Appendix shows a decrease in Q_p^{-1} for increasing elastic and plastic strains, whereas the stress-strain curve shows the presence of a yield point. This behavior is contradicting with the results presented in Figure 8, Figure 9 and Figure 10, where this study found an increase in Q_p^{-1} for increasing plastic strains. In Figure 13 the CT-scan image of Whitby shale sample 47p is presented after deformation.

Figure 13 depicts fractures in the shale sample. In the ZX-plane, all the fractures are concentrated on the left side of the rock sample. In the YX plane, *P*-wave transducer and receiver are placed in the center of the rock sample (in the ZX- and ZY-plane on the top in the middle of the rock sample). Propagating *P*-waves that are travelling through the center are not affected by fractures that are locally concerted at the left side in the ZY-plane. Therefore, an increase in Q_p^{-1} (see the Appendix) for plastic strains is not observed.

To compare the sensitivity of Q_p^{-1} and Q_s^{-1} for the three rock samples during fracturing, $\left(Q_p^{-1}/Q_{p,\max}^{-1}\right)_i$ and $\left(Q_s^{-1}/Q_{s,\max}^{-1}\right)_i$ (i denotes the lithology of the rock sample) are plotted between the yield point and the peak stress as a function of strain in Figure 14. To compare Q_p^{-1} and Q_s^{-1} in the shale samples, Whitby shale samples 22s and 22p are

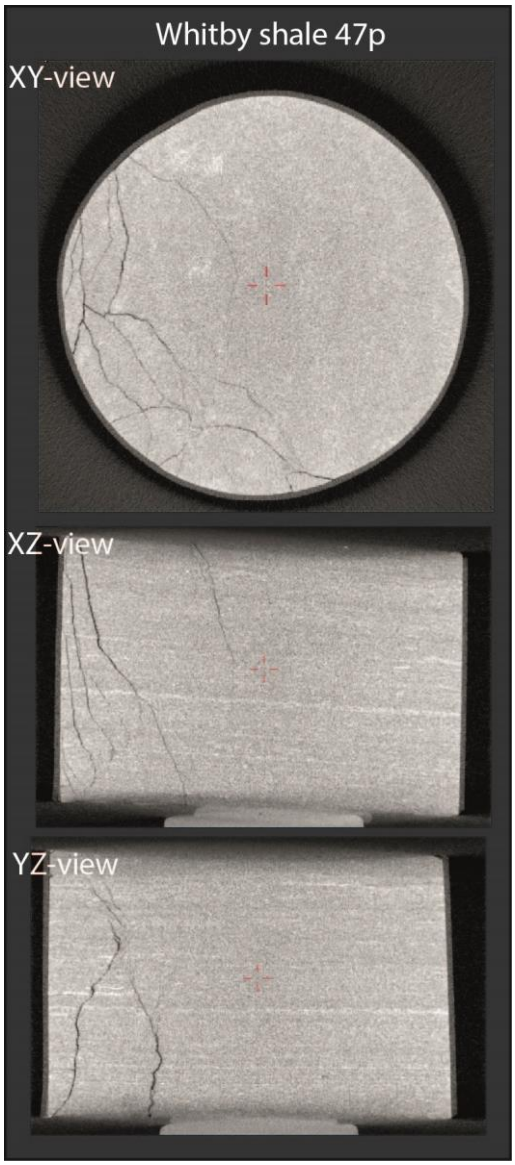

Figure 13: CT-scan images of Whitby shale sample 47p: XY-view (top), XZ-view (middle) and YZ-view bottom).

used. Both rock samples are obtained from the same shale layer (Figure 1) and the rock properties are therefore the most similar.

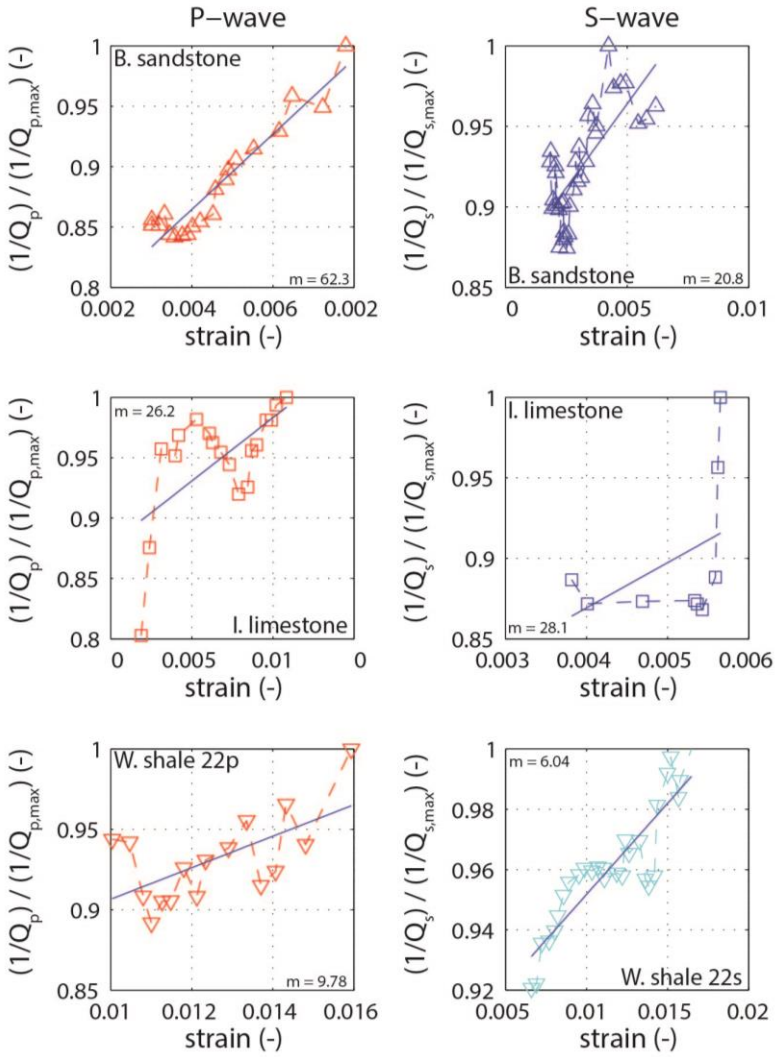

Figure 14: Normalized *P*-wave attenuation (on the left) and *S*-wave attenuation (on the right) plotted between the yield point and the peak stress as a function of strain for Bentheimer sandstone (top), Indiana limestone (middle), and Whitby shales. A linear regression (blue line) is plotted and the regression values (m) are presented in the plot.

In Figure 14 an approximation of $\frac{Q_{p,i}^{-1} / Q_{p,i,\max}^{-1}}{strain}$ and $\frac{Q_{s,i}^{-1} / Q_{s,i,\max}^{-1}}{strain}$ is presented by a linear regression (blue line) and the value of the slope is represented by m. By comparing the values of m, the following observations for all the lithologies about Q_p^{-1} and Q_s^{-1} can be made:

$$\left(\frac{Q_p^{-1} / Q_{p,\max}^{-1}}{strain} \right)_i > \left(\frac{Q_s^{-1} / Q_{s,\max}^{-1}}{strain} \right)_i .$$

For Q_p^{-1} of the different rock samples, the results show:

$$\left(\frac{Q_p^{-1}/Q_{p,\max}^{-1}}{strain}\right)_{sandstone} > \left(\frac{Q_p^{-1}/Q_{p,\max}^{-1}}{strain}\right)_{limestone} > \left(\frac{Q_p^{-1}/Q_{p,\max}^{-1}}{strain}\right)_{shale\ \#22\,p},$$

and for Q_s^{-1}:

$$\left(\frac{Q_s^{-1}/Q_{s,\max}^{-1}}{strain}\right)_{limestone} > \left(\frac{Q_s^{-1}/Q_{s,\max}^{-1}}{strain}\right)_{sandstone} > \left(\frac{Q_s^{-1}/Q_{s,\max}^{-1}}{strain}\right)_{shale\ \#22\,p}.$$

4. Discussion

Rock characteristics found in literature (

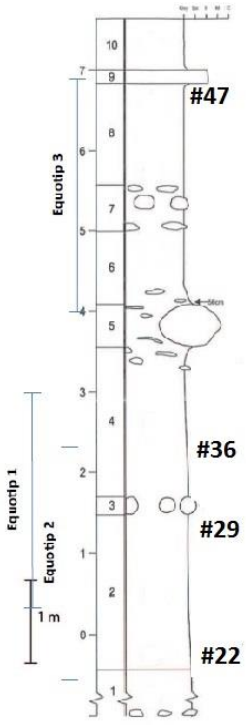

Table 1) and rock characteristics found in this study (Table 2) are in good agreement with each other, in particular for Bentheimer sandstone, which is a homogenous rock. Whitby shale is considered heterogeneous on the scale of investigation, whereas the homogeneity of Indiana limestone is questioned.

The obtained stress-strain relationship for Bentheimer sandstone (Figure 8) with $L/\mathrm{D} \leq 1$ is comparable to those of Ifada [2015], who worked on the same rock sample, but with $L/\mathrm{D} = 2$. In Table 3 the average peak stress ($\bar{\sigma}_{max}$), the average yield stress ($\bar{\sigma}_{yield}$), and the average Young's modulus ($\bar{E}$)of this study and of Ifada [2015] are compared.

Table 3: Comparison of the average peak stress, average yield stress, and average Young's moduli found in this study and in Ifada [2015].

	$\bar{\sigma}_{max}$ (MPa)	$\bar{\sigma}_{yield}$ (MPa)	$\bar{E}$ (GPa)
This study ($L/\mathrm{D} \leq 1$)	58.0±2	36.0±1	18.9±1

Ifada [2015] ($L/\mathrm{D}=2$)	46.1±1	37.3±1	17.4±0.4

The results for $\bar{\sigma}_{max}$ are in agreement with the study of Hawkes and Mellor [1970], who showed that the uniaxial compressive strength decreases as L/D increases. The values of Young's modulus and yield stress of the rock samples in this study differ only very slightly from those of Ifada [2015]. Although $\bar{E}_{L/D\leq 1}$ is bigger and its uncertainty is not in the range of $\bar{E}_{L/D=2}$, the uncertainty of the average yield stress in this study covers the value of Ifada [2015].

For rock samples with $L/\mathrm{D}\approx 2.5$ fractures dominantly occur in the critically stressed zones [*Hawkes and Mellor*, 1970] and are growing to bigger fractures [*Barnhoorn et al.*, 2010] that possibly connect with each other (Figure 2). These zones are not (or to a lesser extent) present in rock samples with $L/\mathrm{D}\leq 1$. Therefore, there are more small fractures homogenously distributed in the rock sample. This study found that the growth of fractures is associated with an increase in attenuation. Seismic waves in a rock sample that contains small fractures are assumed to be less affected than seismic waves in a rock sample that contains big fractures. However, this study shows that seismic waves are significantly affected by these small and homogenously distributed fractures (velocity decrease and attenuation increase). Therefore, the effect of fractures that are concentrated in the critically stressed zones on seismic waves is expected to be bigger in rock samples with $L/\mathrm{D}\approx 2.5$.

For increasing elastic strains, the results in this study show an increase in v_p and v_s and a decrease in Q_p^{-1} and Q_s^{-1}, which is both in agreement with previous studies [*Guo and Fu*, 2007]. Attenuation decreases and velocity increases with increasing effective stress, presumably due to crack closure [*Winkler*, 1982]. Furthermore, this study found that for both *P*-waves and *S*-waves: $v_{limestone} > v_{sandstone} > v_{shale}$ and $(Q_{limestone}^{-1}) > (Q_{sandstone}^{-1}) > (Q_{shale}^{-1})$.

Couvreur et al. [2001] identified the increase in Q_s^{-1} to stable cracking. During fracturing of the rock samples, this study found that Q_p^{-1} and Q_s^{-1} increase with increasing strain and therefore match the observation by Couvreur et al. [2001]. Whitby shale sample 47p in the Appendix shows a decrease in Q_p^{-1} during fracturing. However, CT-scan images reveal that the fractures are concentrated on the edge of the rock sample. Therefore, *P*-waves are not affected by the damage of the rock and an increase in Q_p^{-1} is not observed.

For Bentheimer sandstone an increase in attenuation during fracturing is observed, whereas v_p and v_s are constant. For Indiana limestone and Whitby shale sample 22p, v_p increases during fracturing, which is in agreement with Winkler's study [1979] that has found that attenuation is much more sensitive to increasing elastic stress (and therefore increasing strain) than its velocity.

According to Couvreur et al. [2001], no other parameters except Q_p^{-1} and Q_s^{-1} give indication of the onset of fracturing. By determining the yield point using the stress-strain relationship in combination

with the CT-scan images that contain fractures, this study shows that the yield point is another indicator of the onset of fracturing.

A mercury porosimeter has been used to determine the pore size distribution. Whereas Bentheimer sandstone and Whitby shale sample 47 show a normal pore diameter distribution, Indiana limestone has two dominant pore diameters due to the distribution of fine calcite crystals, which line the pores [*Churcher et al.*, 1991]. Between σ =0 MPa and $\bar{\sigma}_{max}$ the attenuation of Indiana limestone show a decrease, increase, decrease, and increase in attenuation (Figure 9). It is difficult to explain this behavior. Presumably, the first decrease in attenuation can be explained by closing of pores with $d_{limestone}$ =0.7 μm. The first increase in attenuation might be linked to the creation of micro fractures and therefore attenuation increases. The following second decrease in attenuation might be linked to the closing of the big pores with $d_{limestone}$ =19 μm. The second increase in attenuation might then be linked to the creation of (micro) fractures and the growth of these fractures.

To compare Q_p^{-1} and Q_s^{-1} for the three rock samples during fracturing, $\left(\frac{Q_p^{-1}/Q_{p,\max}^{-1}}{strain}\right)_i$ and $\left(\frac{Q_s^{-1}/Q_{s,\max}^{-1}}{strain}\right)_i$ (i denotes the lithology of the rock sample) are compared. This study reveals that Q_p^{-1} is more sensitive to fracturing than Q_s^{-1}. Presumably, this is due to the higher absolute attenuation values of *P*-waves compared to *S*-waves; hence a higher sensitivity for *P*-waves with respect to strain is observed. Additionally, the comparison reveals that attenuation of Whitby shale samples is the least sensitive to fracturing for both *P*-waves and *S*-waves. For Q_p^{-1}, Bentheimer sandstone is more sensitive to fracturing than Indiana limestone and for Q_s^{-1}, Indiana limestone is more sensitive to fracturing than Bentheimer sandstone.

Attenuation in Whitby shale sample 22p is the least sensitive to strain during fracturing: a relatively large compaction is required for only a small increase in attenuation. For an increase in attenuation in Bentheimer sandstone and Indiana limestone, only a relatively small compaction is required. Absolute attenuation values show $(Q_{limestone}^{-1}) > (Q_{sandstone}^{-1}) > (Q_{shale}^{-1})$ for both *P*-waves and *S*-waves.

All the deformation experiments in the Appendix are performed on individual rock samples. There are two sets of rock samples collected from the same shale layer: sample 22p and 22s from layer 22 and sample 47s and 47p from layer 47 (Figure 1), while all the other Whitby shale samples are collected from different shale layers Whitby shales are very heterogeneous and properties such as density, porosity, or velocity can differ greatly layer by layer [*Lie-A-Fat*, 2014; *Ravestein*, 2014]. Density and porosity of Whitby shales can also differ greatly when obtained from the same shale layer as exhibited in Table 2, Comparison of shales is therefore difficult.

To overcome this problem, a transducer that is measuring *P*-waves and *S*-waves at the same time is tested in one rock sample. In the Appendix the results of such a measurement on Indiana limestone is presented. Since there was a large availability of these rock samples, Indiana limestone is used, whereas

the Whitby shales were limited available. The recorded seismic waves contain a high signal-to-noise ratio that made it difficult to pick the first arrival. Additionally, a lot of higher frequencies were recorded that made it hard to use the spectral ratio method and accurately determine attenuation. The recorded seismic waves are filtered by a binomial expansion. Results in Appendix b confirm the observations above: Q_p^{-1} is more sensitive to fracturing than Q_s^{-1}.

In-situ conditions are mimicked by an experimental setup (Figure 3) to measure intrinsic attenuation. However, compared to large-scale heterogeneous structures, the small-scale random heterogeneities in this study, which could be measured by scattering attenuation, may be more sensitive to stress changes [*Guo and Fu*, 2007]. Attenuation inferred from the decay rate of the coda [*Aki and Chouet*, 1975; *Singh and Herrmann*, 1983] is a combination of scattering and intrinsic attenuation. Coda attenuation can therefore be useful for the identification of large-scale heterogeneities and maybe be linked to induced seismicity.

Conventional sonic logs measure only the *P*-wave travel time through the rock formation. Fractures in old wells were identified by cycle skipping caused by the amplitude of the first compressional cycle being too low for detection [*Crain*, 2015]. Nowadays, full waveform acoustic logs are used that contain much more information. Anderson and Walker [1961] and Pickett [1963] suggested amplitude reduction of seismic wave in order to detect fractures.

This research identified the onset of fracturing and the growth of fractures by an increase in Q_p^{-1} and Q_s^{-1}. The decay of the amplitude of seismic waves as a function of time at different stress levels is presented of Whitby shale sample 36s in Figure 15. In Figure 15b, a decay of the amplitude of the seismic wave at the yield stress, $\bar{\sigma}_{yield}$ (red), at the peak stress (blue) and at the stress when the rock sample is completely fractured, $\bar{\sigma}_{fractured}$ (green; Figure 15a) can be observed.

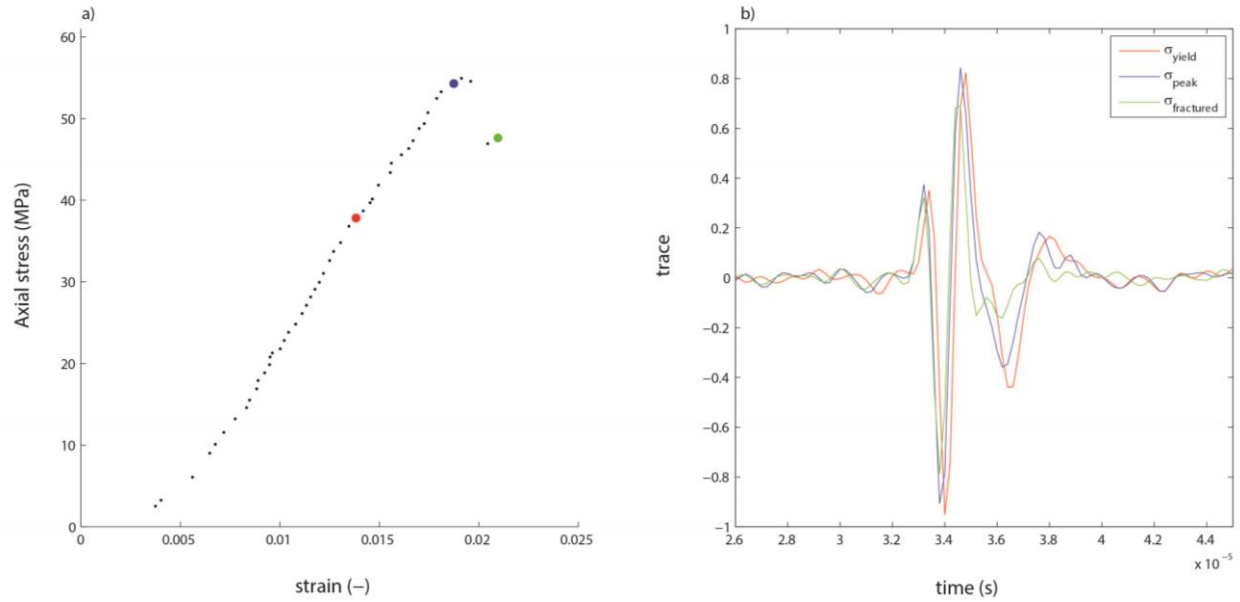

Figure 15: a) Stress-strain relationship of Whitby shale sample 36s. b) Amplitude reduction for different strain levels. Seismic waves are presented for the yield stress, $\bar{\sigma}_{yield}$ (red), for the peak stress (blue) and for the stress when the rock sample is completely fractures, $\bar{\sigma}_{fractured}$ (green).

Other studies have indicated that shear wave amplitudes may be much more sensitive to fractures [*Pickett*, 1963]. Previous work comparing Q_p^{-1} under laboratory conditions to Q_p^{-1} under in-situ conditions found that Q_p^{-1} under laboratory conditions is five times bigger than in Q_p^{-1} under in-situ conditions [*Goldberg and Zinszner*, 1989].

In Figure 16 a simplified diagram of Schlumberger's dipole shear sonic imager (DSI tool) is presented. The DSI tool moves up and down the borehole and records eight full waveforms at different intervals [*Dasios et al.*, 2001]. When an amplitude decay is observed as presented in Figure 15b, one might be able to link this observation to the creation and growth of fractures.

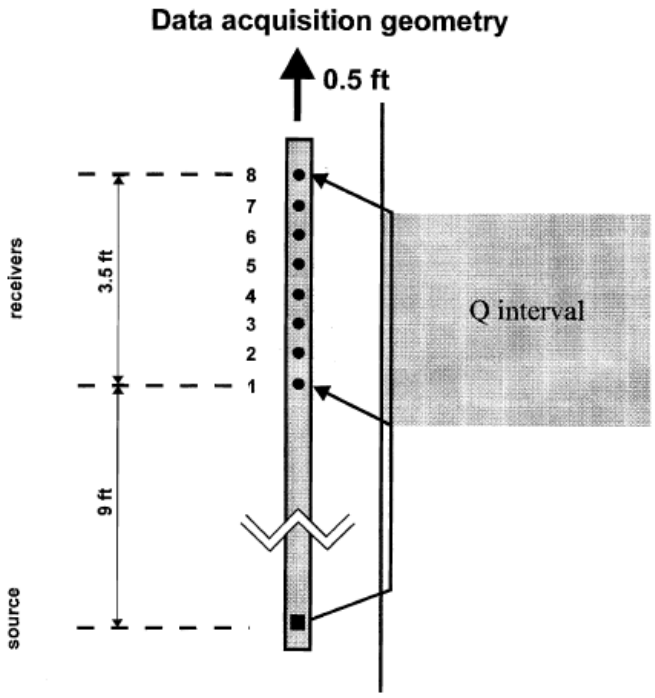

Figure 16: Simplified diagram showing the acquisition geometry of full-waveform sonic data with a long spacing eight-receiver sonic tool (from *Dasios et al.* [2001]).

Therefore, full waveform logs in combination with seismic amplitude reduction may be a powerful tool to detect fractures in boreholes.

5. Conclusions

Seismic wave velocity and seismic wave attenuation in Bentheimer sandstone, Indiana limestone and Whitby shale are studied using a pulse transmission technique at a central frequency of 1 MHz in combination with constantly applied uniaxial stress.

First, the reservoir rocks are characterized by density, porosity, pore size (distribution), and Young's modulus. The rock characteristics that are studied match the values found in literature. Therefore, the studied rock samples are representative for the corresponding lithologies. The rock samples of Bentheimer sandstone are homogenous, Whitby shales are heterogeneous and the homogeneity of Indiana limestone is questioned.

Secondly, the effect of increasing strains on seismic wave velocity and seismic wave attenuation is presented. The primary interest of this study has been to get insights into the behavior of seismic waves when fracturing in rock samples occurs.

For Bentheimer sandstone, Indiana limestone, and Whitby shale, v_p and v_s, whereas Q_p^{-1} and Q_s^{-1} decrease for elastic strains. The yield point is identified as the onset of fracturing of the rock samples and the presence of fractures is confirmed by micro-CT-scan images. Between the onset of fracturing and the peak stress of the rock sample, Q_p^{-1} and Q_s^{-1} increase with increasing plastic strains for all rock types. Additionally, attenuation is more sensitive to fracturing compared to velocity.

Furthermore, the attenuation of the lithologies is compared to each other. For the absolute attenuation values (*P*-wave and *S*-wave) the following inequality applies: $(Q_{limestone}^{-1}) > (Q_{sandstone}^{-1}) > (Q_{shale}^{-1})$. Concerning the sensitivity of attenuation to increasing strains during fracturing, *P*-wave attenuation in Bentheimer sandstone is more sensitive to fracturing compared to attenuation in Indiana limestone. *P*-wave attenuation in Whitby shale samples are the least sensitive to fracturing. The sensitivity study for *S*-waves identified attenuation in Indiana limestone as bigger than that in Bentheimer sandstone and S-wave attenuation in Whitby shale sample is the least sensitive to fracturing. Additionally, Q_p^{-1} is more sensitive to fracturing compared to Q_s^{-1}. At last, full waveform recorded logs in combination with seismic amplitude reduction might be a powerful tool to detect fractures in boreholes.

References

Aki, K., and B. Chouet (1975), Origin of coda waves: Source, attenuation, and scattering effects, *J. Geophys. Res.*, *80*(23), 3322, doi:10.1029/JB080i023p03322.

Anderson, W. L., and T. Walker (1961), Application of open hole acoustic amplitude measurements, *SPE*, *122*.

Barnhoorn, A., S. F. Cox, D. J. Robinson, and T. Senden (2010), Stress- and fluid-driven failure during fracture array growth: Implications for coupled deformation and fluid flow in the crust, *Geology*, *38*(9), 779–782, doi:10.1130/G31010.1.

Boogaert, A., and W. F. P. Kouwe (1993), *STRATIGRAPHIC NOMENCLATURE OF THE NETHERLANDS*.

Britt, L. K., and J. Schoeffler (2009), The Geomechanics Of A Shale Play: What Makes A Shale Prospective!, *SPE*, *Paper 1255*(September 2009), 1–9, doi:10.2118/125525-MS.

Chichinina, T., V. Sabinin, and G. Ronquillo-Jarillo (2006), QCOA analysis: P-wave attenuation anisotropy for dracture characterization, *Geophysics*, *71*(3), C37–C48.

Christensen, N. I., and H. F. Wang (1985), The influence of pore pressure and confining pressure on dynamic proporties of Barea sandstone, *Geophysics*, *50*(2), 207–213.

Churcher, P. L., P. R. French, J. W. Shaw, and L. L. Schramm (1991), Rock Properties of Berea Sandstone, Baker Dolomite, and Indiana Limestone, *SPE*, (International Symposium on Oilfield Chemistry), 431–466, doi:10.2118/21044-MS.

Couvreur, J. F., A. Vervoort, M. S. King, E. Lousberg, and J. F. Thimus (2001), Successive cracking steps of a limestone highlighted by ultrasonic wave propagation, *Geophys. Prospect.*, *49*(1), 71–78, doi:10.1046/j.1365-2478.2001.00242.x.

Crain, E. R. (2015), CRAIN'S PETROPHYSICAL HANDBOOK -FRACTURE IDENTIFICATION from SONIC LOGS, Available from: https://www.spec2000.net/22-fracloc4.htm (Accessed 12 July 2015)

Dasios, A., T. R. Astin, and C. McCann (2001), Compressional-wave Q estimation from full-waveform sonic data, *Geophys. Prospect.*, *49*(3), 353–373, doi:10.1046/j.1365-2478.2001.00259.x.

Goldberg, D., and B. Zinszner (1989), P-wave attenuation measurements from laboratory resonance and sonic waveform data, *Geophysics*, *54*(1), 76–81, doi:10.1190/1.1442579.

Google-Earth (2015), Goolge Earth image of coast near port Mulgrave,

Guo, M. Q., and L. Y. Fu (2007), Stress associated coda attenuation from ultrasonic waveform measurements, *Geophys. Res. Lett.*, *34*(9), 1–5, doi:10.1029/2007GL029582.

Hawkes, I., and M. Mellor (1970), Uniaxial testing in rock mechanics laboratories, *Eng. Geol.*, *4*(3), 179–285, doi:10.1016/0013-7952(70)90034-7.

Houben, M., A. Barnhoorn, M. Drury, C. Peach, and C. Spiers (2015), Microstructure and permeability of the Whitby Mudstone (UK) as an analogue for the Posidonia shale (NL), vol. 17, p. 4654.

Ifada, M. (2015), Fracture mode analyses, Geomechanics Petrophysics, and Fracture Characterization: An Experimental Investigaion on Whitby Shales and Various Other Rock Types, Delft University of Technology.

INDIANA-LIMESTONE-INSTITUTE-OF-AMERICA (2007), *Indiana Limestone handbook*, 22nd ed.

Khaksar, A., C. M. Griffiths, and C. McCann (1999), Compressional- and shear-wave velocities as a function of confining stress in dry sandstones, *Geophys. Prospect.*, *47*(4), 487–508, doi:10.1046/j.1365-2478.1999.00146.x.

Klein, E., P. Baud, T. Reuschlé, and T. F. Wong (2001), Mechanical behaviour and failure mode of Bentheim sandstone under triaxial compression, *Phys. Chem. Earth, Part A Solid Earth Geod.*, *26*(1-2), 21–25, doi:10.1016/S1464-1895(01)00017-5.

Kocourek-Industries (2013), Indiana limestone, Available from: http://www.kocurekindustries.com/indiana-limestone-70mD-cores (Accessed 15 May 2015)

Lie-A-Fat, J. W. . (2014), Microstructural, Petrophysical and Anisotropy Analysis of a Posidonia Shale Analogue, Delft University of Technology.

Lockner, D. a., J. B. Walsh, and J. D. Byerlee (1977), Changes in seismic velocity and attenuation during deformation of granite, *J. Geophys. Res.*, *82*(33), 5374, doi:10.1029/JB082i033p05374.

Lucet, N., and B. Zinszner (1991), Effects of heterogeneity and anisotropy in sonic and ultrasonic attenuation in rocks, *Geophysics*, *57*(8), 1018–1026.

Maloney, D. R., M. M. Honarpour, and A. D. Brinkmeyer (1990), The effects of rock characteristics on relative permeability, , 29.

Maultzsch, S., M. Chapman, E. Liu, and X. Y. Li (2003), Modelling frequency-dependent seismic anisotropy in fluid-saturated rock with aligned fractures: Implication of fracture size estimation from anisotropic measurements, *Geophys. Prospect.*, *51*(5), 381–392, doi:10.1046/j.1365-2478.2003.00386.x.

Maultzsch, S., M. Chapman, E. Liu, and X. Y. Li (2007), Modelling and analysis of attenuation anisotropy in multi-azimuth VSP data from the Clair field, in *Geophysical Prospecting*, vol. 55, pp. 627–642.

Mavko, G. M., and A. Nur (1979), Wave attenuation in partially saturated rocks, *Geophysics*, *44*(2), 161–178, doi:10.1190/1.1440958.

Miller, S. A., and A. L. Florence (1991), *Laboratory Particle velocity experiments on Indiana limestone and Sierra white granite*, Hanscom air force base, Massachuetts.

Paterson, M. S., and T. Wong (2005), *Experimental Rock Deformation — The Brittle Field*, Second., Springer.

Pickett, G. R. (1963), Acoustic Character Logs and Their Applications in Formation Evaluation, *J. Pet. Technol.*, *15*(6), 659–667, doi:10.2118/452-PA.

Ravestein, T. (2014), Fraccability determination of a Posidonia Shale Formation analogue through geo-mechanical experiments and micro-CT fracture propagation analysis, Delft University of Technology.

Samec, P., and J. P. Blangy (1992), Viscoelastic attenuation, anisotropy, and AVO, *Geophysics*, *57*(March), 441–450.

Scott, T. E., Q. Ma, and J. C. Roegiers (1992), Acoustic Velocity Changes During Shear Enhanced Compaction of Sandstone, *Int. J. Rock Mech. Min. Sci. Geomech. Abstr.*, *30*(7), 763–769, doi:10.1016/0148-9062(93)90020-E.

Singh, S., and R. B. Herrmann (1983), Regionalization of Crustal Coda Q in the Continental United States, *J. Geophys. Res.*, *88*(B1), 527–538, doi:10.1029/JB088iB01p00527.

Stanchits, S., S. Vinciguerra, and G. Dresen (2006), Ultrasonic velocities, acoustic emission characteristics and crack damage of basalt and granite, in *Pure and Applied Geophysics*.

Taylor, J. R. (1982), *An introduction to error analysis the study of uncertainties in physical measurements*, Second., University Science Books Sausalito, California.

Tocher, D. (1957), Anisotropy in Rocks under Simple Compression, *Am. Geophys. Union*, *38, No. 1*.

Winkler, K. W. (1979), THe effect of pore fluid and fritional sliding on seismic attenuation, Stanford University.

Winkler, K. W. (1982), Seismic attenuation: Effects of pore fluids and frictional-sliding, *Geophysics*, *47*(1), 1, doi:10.1190/1.1441276.

Zhubayev, A., and A. Barnhoorn (2013), *Seismic Anisotropy of Posidonia Shale* .

Zijp, M. (2012), *Schaliegas in Nederland*.

Zijp, M. (2013), *Oil and Gas in the Netherlands*.

Appendix

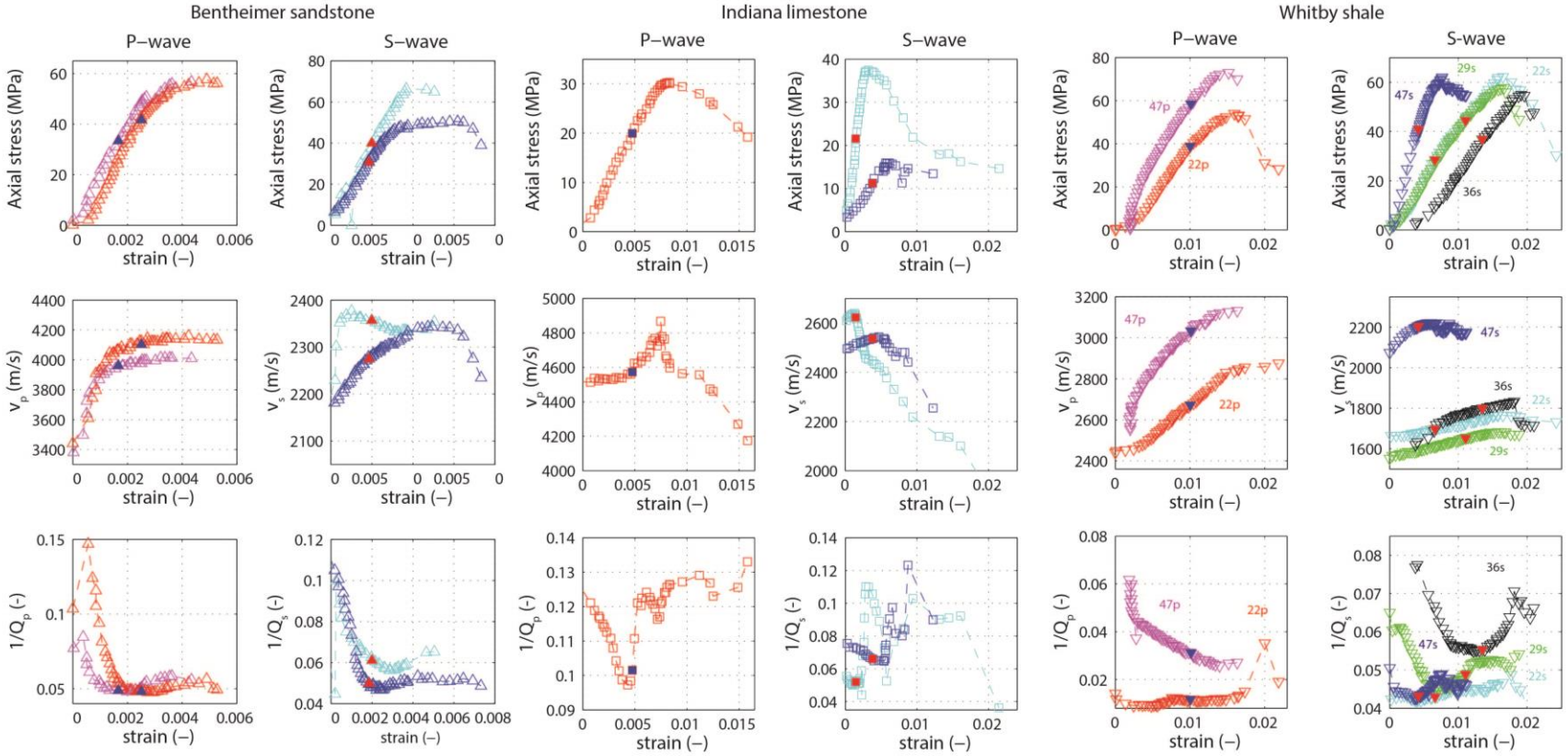

Appendix a: From top to bottom: Axial stress, *P*-wave *and* *S*-wave velocity and *P*-wave *and* *S*-wave attenuation as a function of strain. From left to right: Result of Bentheimer sandstone, Indiana limestone, and Whitby shale samples.

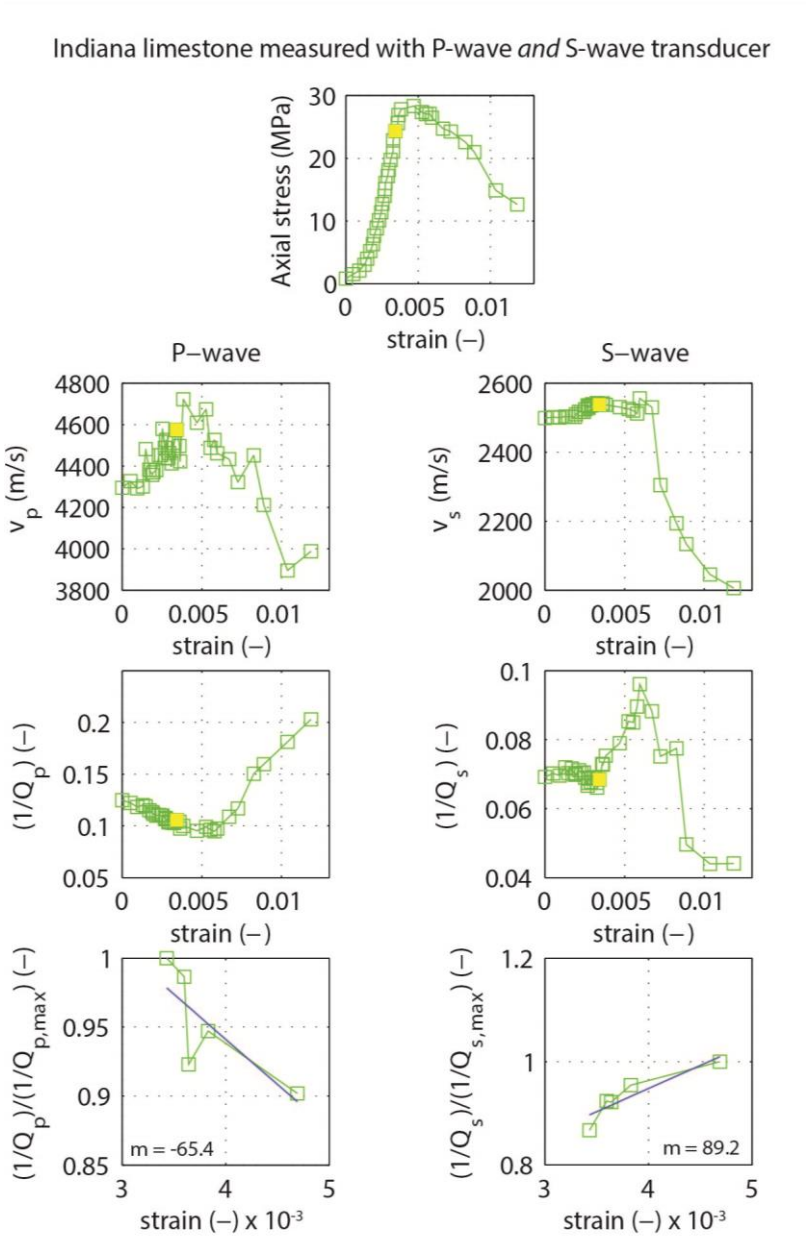

Appendix b: Axial stress, *P*-wave velocity (left), *S*-wave velocity (right), *P-wave* and *S*-wave attenuation and sensitivity plots (bottom) during fracturing of Indiana limestone as a function of strain.